

The distribution of the coronal temperature in Seyfert 1 galaxies

A. Akylas¹ and I. Georgantopoulos¹

Institute for Astronomy Astrophysics Space Applications and Remote Sensing (IAASARS), National Observatory of Athens, I. Metaxa & V. Pavlou, Penteli, 15236, Greece
e-mail: aakylas@noa.gr

August 26, 2021

ABSTRACT

The Active Galactic Nuclei (AGN) produce copious amounts of X-rays through the corona that is the hot gas that lies close to the accretion disk. The temperature of the corona can be accurately determined by the cut-off signature in the X-ray spectrum. Owing to the large temperatures of the corona, observations well above 10 keV are necessary. Here, we explore the *NuSTAR* observations of 118 *Gehrels/Swift* selected Seyfert 1 AGN. We model the spectrum using a single power-law with an exponential cut-off modified by neutral and ionised absorption as well as a reflection component. We find secure spectral cut-off estimates in 62 sources while for the remaining ones we derive only lower limits. The mean value is 103 keV with a skewed distribution towards large energies with large dispersion. When we consider the lower limits using survival analysis techniques, the mean cut-off energy becomes significantly larger, about 200 keV. Because of various limitations (e.g. limited spectral passband, photon statistics, model degeneracies) we perform extensive simulations to explore the underlying spectral cut-off distribution. We find that an intrinsic spectral cut-off distribution which has a Maxwell-Boltzmann shape with a mean value in the range of 160 - 200 keV can reproduce sufficiently well the observations. Finally, our spectral analysis places very stringent constraints on both the photon index ($\Gamma = 1.77 \pm 0.01$) as well as on the reflection component ($R = 0.69 \pm 0.04$) of the Seyfert 1 population. From the values of the spectral cut-off and the photon-index we deduce that the mean optical depth of the AGN corona is approximately $\tau_e = 1.82 \pm 0.14$ and its mean temperature approximately $kT_e = 65 \pm 10$ keV.

Key words. X-rays: general – galaxies: active – catalogs – quasars: supermassive black holes

1. Introduction

Accreting SMBH (Supermassive Black Holes) or AGN (Active Galactic Nuclei) produce large amounts of radiation primarily in the UV and optical wavelengths. This radiation is believed to be produced in an optically thick accretion disk formed by material infalling to the black hole. X-ray radiation is a ubiquitous feature of AGN (Brandt & Alexander 2015). The X-ray continuum is produced in a region of hot plasma called the corona. The X-rays are produced as the hot electrons scatter the UV photons coming from the accretion disk through inverse Compton scattering (Vaiana & Rosner 1978; Haardt & Maraschi 1991). The rapid X-ray variability observed (e.g. McHardy et al. 2005; Ludlam et al. 2015), as well as reverberation of the X-ray radiation reprocessed by the accretion disk, the so-called reflection component, (Emmanoulopoulos et al. 2014; Uttley et al. 2014; Kara et al. 2016) suggest that the corona is small in size (several times the gravitational radius of the black hole). These findings have been confirmed by microlensing studies (e.g. Chartas et al. 2016; Guerras et al. 2017).

Broad-band X-ray spectroscopy of the X-ray emission can provide important constraints on the physical parameters of the coronal gas. In particular, the temperature kT_e in combination with the optical depth τ_e determines the slope of the power-law spectrum (e.g. Petrucci et al. 2001). The higher the optical depth, the flatter the X-ray continuum at a given temperature of the corona. The X-ray broad-band spectrum is usually parameterised as $E^{-\Gamma} e^{-E/E_c}$ where E is the photon energy, Γ the photon index and E_c is the spectral energy cut-off that accurately measures the temperature of the corona. However, it is challenging to deter-

mine the value of the the spectral cut-off as this requires observations well above 10 keV. The spectral cut-off has been measured directly for the first time using the *Compton Gamma-ray* observatory. It has been found that the spectral cut-off in NGC4151 is around 100 keV (Johnson et al. 1997). The *BeppoSAX* mission increased the number of the spectral cut-off measurements (Dadina 2007). More recently, a large number of observations has been accumulated using either the *INTEGRAL* or the *Gehrels SWIFT* missions. Malizia et al. (2014) presented the *INTEGRAL* spectra of a sample of Seyfert 1 galaxies detecting securely the cut-off energy in 26 sources. They find an average high energy cut-off of 128 keV with a standard deviation of 46 keV. Ricci et al. (2017) presented the most comprehensive X-ray spectral analysis of AGN in the local Universe. They presented the X-ray spectra of all the AGN detected in the *Gehrels SWIFT/BAT* survey. There are 352 unobscured AGN ($N_H < 10^{22} \text{cm}^{-2}$). In 89 sources the spectral cut-off could be securely inferred (no censored values, i.e. upper or lower limits) with a mean value of 80 ± 7 keV. Taking into account all sources i.e. including lower and upper limits by means of survival analysis techniques, they find a mean cut-off energy of 331 ± 29 keV. This value is substantially higher than that derived by Malizia et al. (2014).

The launch of the *NuSTAR* mission (Harrison et al. 2013) brought a leap forward in the study of the high energy spectra of AGN owing to its excellent spatial resolution above 10keV. *NuSTAR* observations of the cut-off of AGN include Fabian et al. (2015), Kamraj et al. (2018), Molina et al. (2019), Rani et al. (2019). Molina et al. (2019) analysing a sample of 18 Seyfert 1 galaxies, 13 secure measurements plus five lower limits, find a mean value for the cut-off of $E_c = 111$ keV with a dispersion

of 45 keV. Rani et al. (2019) present a sample of eight Seyfert 1 AGN with securely derived cut-off. This sample yields a mean cut-off value of 95 keV with a dispersion of 32 keV. Finally, Baloković et al. (2020) presented the *NuSTAR* spectra of 130 Seyfert 2 galaxies selected by *Gehrels SWIFT*. They find a median cut-off of 290 ± 20 keV.

It becomes evident that there are still significant uncertainties in the value of the spectral cut-off and hence the temperature of the corona. This is partly because of the presence of a considerable fraction of lower limits among some of the above samples. Moreover, there is a considerable spread in the values of the cut-offs even among the securely constrained values. It is not clear whether this large spread reflects the intrinsic dispersion of AGN coronal temperatures or alternatively it can be attributed to the limited photon statistics and the relatively limited pass-band of even the hard-energy detectors. In this paper we are trying to overcome this impasse by exploring the X-ray spectroscopic analysis, with *NuSTAR*, of the largest sample of Seyfert 1 galaxies presented so far. The Seyfert 1 sample comes from the 107-month *Gehrels SWIFT/BAT* sample of Oh et al. (2018). Our primary goal is to derive the intrinsic X-ray spectral cut-off distribution. A key feature of our analysis is that we present detailed simulations in order to take into account all systematics that affect the determination of the spectral cut-off. Together with the robust estimation of the spectral cut-off, our spectral modelling provides strong constraints on the photon index distribution as well as on the strength of the reflection component. Throughout the paper, we adopt the standard cosmological parameters $H_0 = 70 \text{ km s}^{-1} \text{ Mpc}^{-1}$, $\Omega_m = 0.3$, $\Omega_\Lambda = 0.7$.

2. The sample

Here we compile the archival Nuclear Spectroscopic Telescope Array (*NuSTAR*) observations of the Seyfert 1 galaxies detected in the 105-month survey of the Burst Alert Telescope, BAT, (Barthelmy 2004) survey on-board the *Gehrels Swift* Gamma-Ray Burst observatory (Gehrels et al. 2004). The 105-month BAT survey (Oh et al. 2018) is a uniform, hard X-ray, all-sky survey with a sensitivity of $8.40 \times 10^{-12} \text{ erg s}^{-1} \text{ cm}^{-2}$ over 90% of the sky and $7.24 \times 10^{-12} \text{ erg s}^{-1} \text{ cm}^{-2}$ over 50% of the sky, in the 14–195 keV band. The BAT 105 month catalogue provides 1632 hard X-ray sources in the 14–195 keV band above the 4.8σ significance level. Frequently, since its start of operations in 2012, the *NuSTAR* satellite has been taking observations of AGNs selected from the *Gehrels Swift/BAT* hard X-ray catalogue.

NuSTAR, (Harrison et al. 2013) launched in June 2012, is the first orbiting X-ray observatory which focuses light at high energies ($E > 10$ keV). It consists of two co-aligned focal plane modules (FPMs), which are identical in design. Each FPM covers the same 12×12 arcmin portion of the sky, and comprises of four Cadmium-Zinc-Tellurium detectors. *NuSTAR* operates between 3 and 79 keV and provides an improvement of at least two orders of magnitude in sensitivity compared to previous hard X-ray observatories operating at energies $E > 10$ keV. We take advantage of the *NuSTAR* unprecedented sensitivity above 10 keV to measure, the distribution of the high energy cut-off of the Seyfert 1 population in the local universe.

In the 105 months *Gehrels Swift/BAT* hard X-ray catalogue there are in total 370 Seyfert 1 galaxies including type 1.0 (163 AGN) type 1.2 (96 AGN) and type 1.5 (111 AGN). Up until recently, there have been observed in total 142 of these *Gehrels Swift/BAT* Seyfert 1 with *NuSTAR*. Note that the majority of the sources observed by *NuSTAR* belong to the 70-month BAT catalogue (Baumgartner et al. 2013) while only an additional four

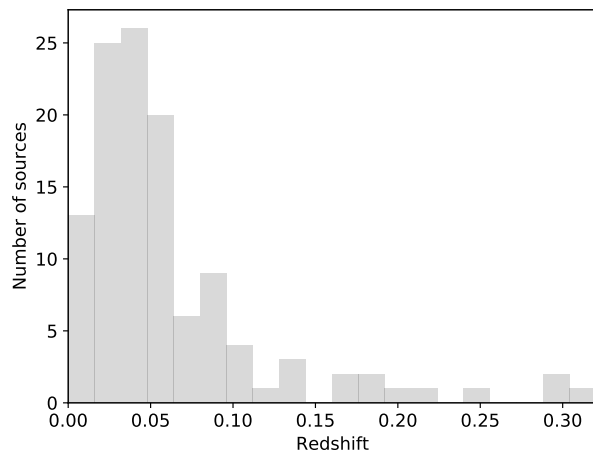


Fig. 1. The redshift distribution of the 122 sources in the final sample.

come from the 105 month catalogue. The effective energy range of *NuSTAR* detectors (3–79 keV) does not allow an accurate measurement of the lower N_H hydrogen column densities. Despite the fact that *NuSTAR* is not sensitive to soft X-rays below 3 keV, even moderate column densities could easily absorb the X-ray photons within its pass-band. For example assuming a power-law spectrum with a photon index $\Gamma = 1.8$, a column density of $N_H = 10^{22} \text{ cm}^{-2}$ reduces the *NuSTAR* flux in the 3–10 keV band by ~ 4 per cent. If the column density N_H becomes $5 \times 10^{22} \text{ cm}^{-2}$ then the reduction of the 3–10 keV flux becomes ~ 18 per cent. In order to minimize the effect of the photo-electric absorption at the lower part of the X-ray spectrum we focus only on the X-ray unobscured Seyfert 1 galaxies (i.e. $N_H < 1 \times 10^{22} \text{ cm}^{-2}$). This is important since the degeneracy between the photon index and the column density may affect the cut-off energy measurements.

Ricci et al. (2017) have provided accurate measurements of the X-ray absorption by using *XMM-Newton*, *Swift/XRT*, *ASCA*, *Chandra*, and *Suzaku* observations in the soft X-ray band (< 10 keV) with the 70-month averaged *Swift/BAT* data. Based on their results we exclude from the analysis 20 sources showing $N_H > 1 \times 10^{22} \text{ cm}^{-2}$. Our final sample comprises of 122 sources. The observational details of the sample are listed in Table 1 in increasing BAT obsID order. The source name, redshift and the optical classification type has been obtained from the 105-month BAT survey catalogue. The *NuSTAR* observation identifier used in the analysis is also shown. When multiple observations are present we choose to analyze the observation with the highest exposure. Last, the net counts of each observation calculated from the combined (FMPA and FMPB) observations are also presented.

3. X-ray spectral analysis

3.1. X-ray spectral reduction

Spectral reduction has been performed for both *NuSTAR* modules, FPMA, and FPMB, using the *NuSTAR* Data Analysis Software (NuSTARDAS; version 1.2.1), within the HEASOFT (version 6.16). We have extracted source and background energy spectra from the calibrated and cleaned event files using the NUPRODUCTS module. Detailed information on the data reduction procedures can be found in the *NuSTAR* Data Analysis Software Guide (Perri et al. 2017). An extraction radius of $60''$ has

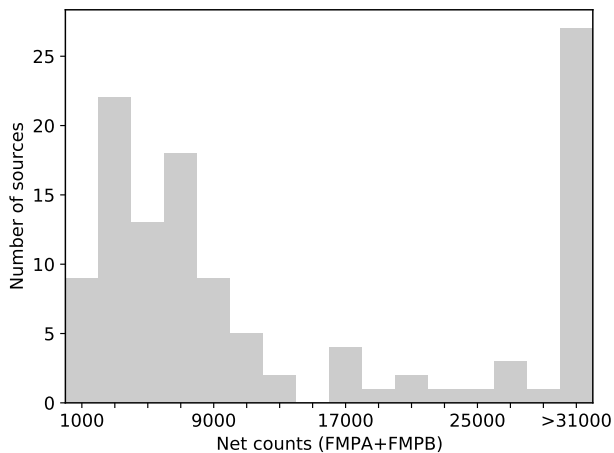


Fig. 2. The background subtracted count distribution of our observations from the combined FPMA and FPMB instruments. The minimum number of counts is 550 and the maximum number is 697782 counts.

been used for both the source and background regions. The background spectrum has been estimated from several source-free regions of the image at an off-axis angle similar to the source position. The spectral files were re-binned using the HEASOFT task GRPPHA to give a minimum of 20 photon counts per bin. In Fig. 1 we present the background subtracted count distribution of our observations from both FPMA and FPMB instruments to depict the excellent statistical quality of the spectra. The minimum number of the background subtracted (FMPA & FMPB) counts is 550 and corresponds to the source with BAT obsID 495 while BAT source 694 show the maximum number of 697782 counts.

3.2. Spectral fitting

The spectral fitting is carried out using XSPEC v12.8.2 (Arnaud 1996). We simultaneously fit the spectra from both the FMPA and FMPB instruments. We fit the data using the PEXMON model in XSPEC (Nandra et al. 2007). This describes an exponentially cut-off power-law spectrum, reflected by a neutral material slab and takes into account the self-consistently generated narrow Fe K lines. The relative reflection strength is parameterised by R , where $R=1$ corresponds to a semi-infinite slab seen at an inclination angle of θ and subtends a 2π solid angle at the X-ray source. We take both neutral and ionized absorption into account. Although we have already discarded all sources with absorption above 10^{22}cm^{-2} as found by Ricci et al. (2017), we check for possible variability in the column densities. The neutral absorption column density is modeled using the ZPHABS model in XSPEC. Regarding ionised absorption, the hard spectral band of *NuSTAR* which excludes energies below 3 keV, does not allow us to easily constrain any possible ionised absorption features. Using softer X-ray data, Ricci et al. (2017) find evidence for ionised absorption in 33 sources from our sample. This was found using the ZXIPCF model (Reeves et al. 2008) which uses a grid of XSTAR absorption models (Kallman & Bautista 2001). We fix the setting of the ionised absorption values to those derived by Ricci et al. (2017). Following Ricci et al. (2017) and since we are primarily interested on the spectral cut-off, we chose for simplicity to model the Fe line emission only using a narrow component. Then, our modelling of the Fe emis-

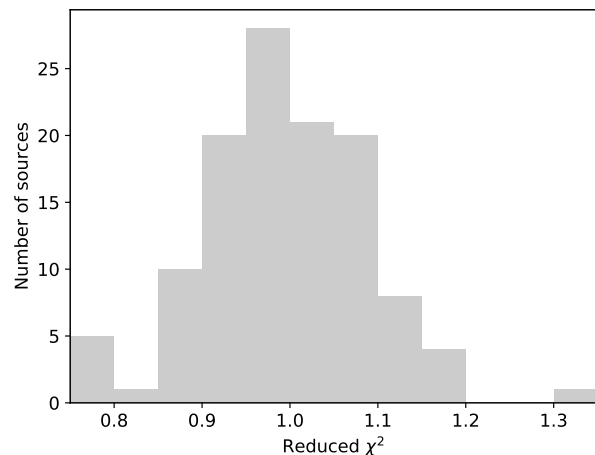


Fig. 3. The reduced χ^2 (χ^2 over degrees of freedom) for all sources.

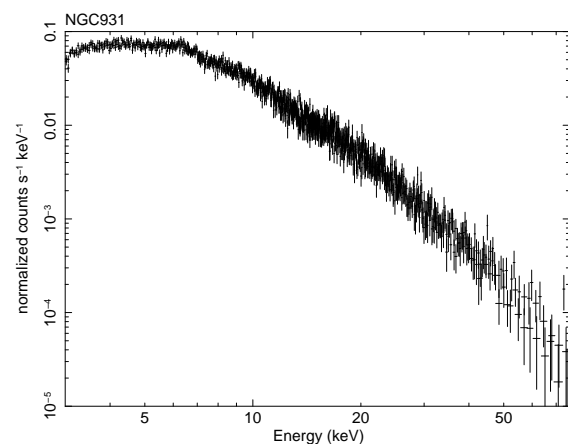


Fig. 4. The spectrum of the source NGC931.

sion relied on the PEXMON model and we do not add a broad Fe line component. Finally, a constant multiplication factor, varying within 3 per cent between FMP instruments, has also been included to account for calibration issues. In XSPEC notation our model is described as: ZPHABS*ZXIPCF*PEXMON. The inclination angle of the reflecting slab has been frozen to 60 degrees. The photon index (Γ), the relative reflection strength (R), the high energy cutoff (E_c) and the normalization parameters are free to vary. We use χ^2 statistics for goodness of fitting and error estimation.

In Fig. 3 we show the distribution of the reduced χ^2 (χ^2 over degrees of freedom) for all our spectra. In order to demonstrate the excellent quality of the photon statistics we present as an example the spectrum of the source NGC931 in Fig. 4.

4. Results

In Table 2 we present all the spectral fitting results for each source and the corresponding BAT ObsID, in increasing order, to facilitate direct comparison with the information listed in Table 1. All the errors in the spectral components correspond to the

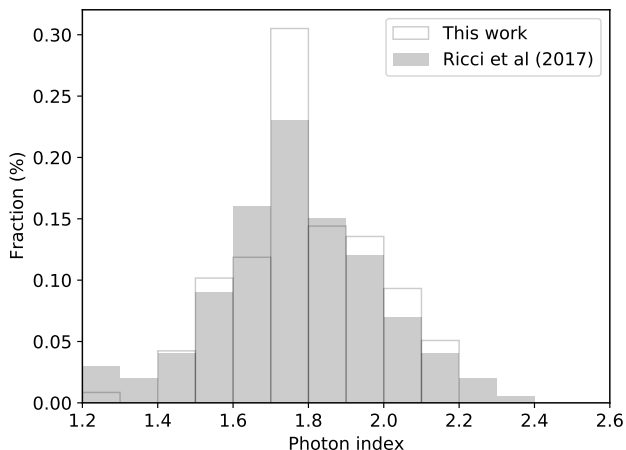


Fig. 5. Distribution of the photon indices (open histogram). The gray histogram shows the estimates from Ricci et al. (2017). The distributions are normalized to facilitate the comparison.

90 per cent confidence interval. The estimated flux and luminosity are also presented for both the soft (2-10 keV) and the hard (20-40 keV) bands.

4.1. Absorption

Although we omitted from our sample all sources with column density $N_{\text{H}} > 10^{22} \text{ cm}^{-2}$ as estimated in Ricci et al. (2017), our spectral fitting revealed four sources that present significant absorption ($> 5 \times 10^{22} \text{ cm}^{-2}$) in the *NuSTAR* spectra. These are the sources with BAT obsID 449, 765, 912 and 976. As all these appear unobscured in Ricci et al. (2017) analysis, this suggests significant variability in the obscuring screen. At least for the case of Mrk704, such evidence have been presented previously in e.g. Matt et al. (2011). Following our selection criteria, discussed in Section 2 we exclude these four sources from further analysis, leaving 118 sources in our sample.

4.2. Photon index

The photon index has been accurately measured for all 118 sources with no upper or lower limit measurements. The normalized distribution is presented in Fig. 5. The median (mean) value of the photon index distribution is 1.77 (1.78). The upper and lower quartiles are 0.13 and 0.14 respectively. We can approximate the 90 per cent error of the median (mean) using the relations $\sigma_{\text{mean}} = \sqrt{(\sum(\delta\Gamma_i)^2)/N}$ and $\sigma_{\text{median}} = k \times \sigma_{\text{mean}}$. The scaling factor k equals 1.253 assuming a Gaussian distribution and $\delta\Gamma_i$, the individual errors in the photon index, can be approximated by the average value of upper and lower limit uncertainties. Then the corresponding median (mean) error is $\sigma=0.013$ (0.010).

Ricci et al. (2017) presented the broadband X-ray characteristics of the 70-month *Swift*/BAT all-sky survey by combining BAT AGN spectra with deeper soft X-ray observations. Their best-fitting photon indices for non-blazar AGNs with $N_{\text{H}} < 10^{22} \text{ cm}^{-2}$ have also been plotted for comparison in Fig. 5. They find a median $\Gamma = 1.80 \pm 0.02$. Both the median value and the full distribution are in excellent agreement with our findings.

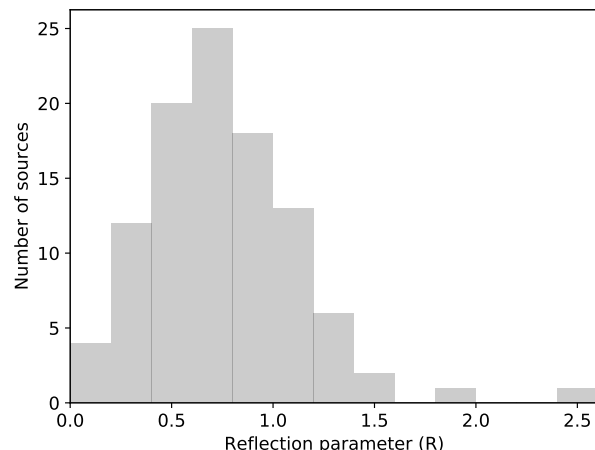


Fig. 6. Distribution of the reflection parameter R for the 106 sources in our sample.

4.3. Reflection parameter

The reflection parameter R, has been securely inferred (no censored values) for 106 out of 118 sources. For 12 sources (~ 13 per cent of the sample) only upper limits could be obtained for R. In these cases the R value in Table 2 corresponds to the 90 per cent upper limit. In Fig. 6 we plot the distribution of the reflection parameter for the 106 sources. The median (mean) value is 0.71 (0.66). The first and third quartiles are 0.49 and 0.91 respectively. Using the same assumptions as in the case of the photon index the error on the median (mean) value is $\sigma=0.06$ (0.05). Next, we derive the reflection parameter, taking all 118 sources into account i.e. including the lower limits. We use the survival analysis ASURV software package (Isobe et al. 1986).

The derived corrected mean value from ASURV is $R = 0.69 \pm 0.04$. Ricci et al. (2017) obtain a median R value of 0.83 ± 0.14 taking into account all measurements for their $N_{\text{H}} < 10^{22} \text{ cm}^{-2}$ sample. This is in reasonable agreement with our estimates. However, the present *NuSTAR* results offer a substantial qualitative improvement over the previous BAT results. This is because there is a significant fraction of lower limits in Ricci et al. (2017) while in our sample it is very low (13 per cent).

4.4. The high energy cut-off

The high energy cut-off parameter, E_c , has been securely measured for 62 sources (53 per cent of sample). For the remaining 56 sources we provide the 90 per cent lower limit. The highest E_c value of $334^{+646}_{-140} \text{ keV}$ measured in NGC1566, demonstrates the ability of *NuSTAR* to constrain even some highest energy cut-offs. NGC4051 possibly represents another case of a cut-off at very high energies. Despite the lower-limit E_c estimate for NGC4051, the results suggest a high energy cut-off greater than $\sim 700 \text{ keV}$ at a 90 per cent confidence. Given the excellent quality of the spectrum, presenting more than 200,000 net counts, this suggests an extremely high value for E_c similar for example to the Seyfert 2 NGC5506 (Matt et al. 2015).

In Fig. 7 we plot the distribution of the high energy cut-off for the 62 sources with securely inferred spectral cut-offs. The median (mean) value is 89 (102) keV. The first and third quartiles are 65 keV and 102 keV respectively. Using the same assump-

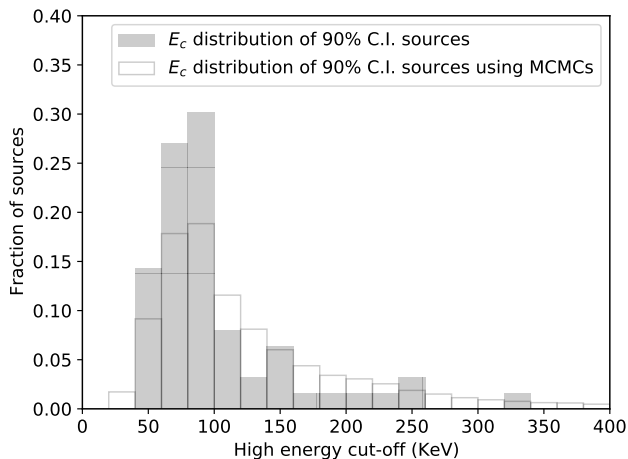


Fig. 7. Grey histogram: The observed distribution of the high energy spectral cut-off for the 62 sources with securely inferred values. White histogram: The same population with the grey histogram after taking into account the uncertainties in each individual measurement of the E_c parameter using MCMC simulations.

tions as in the case of the photon index and R the approximated error on the median (mean) value is $\sigma=20$ (16) keV. We note that Ricci et al. (2017) finds a median value 80 keV for their securely inferred E_c measurements, fully comparable to our result. Since for a large fraction of our sources in our sample ($\sim 50\%$) only lower limits on the high energy cut-off are available, the values reported above are not representative of the whole sample of Swift/BAT AGN. Therefore we use the Kaplan-Meier estimator (Isobe et al. 1986) in order to take the upper and lower limits into account. We find a mean value of 206 ± 38 keV. Ricci et al. (2017) quote a mean value of 331 ± 29 keV. The striking difference of the results possibly relates to the substantial fraction of censored values in the sample of Ricci et al. (2017) (i.e. $>70\%$).

Nevertheless, Fig. 7 suggests that the E_c distribution is right-skewed. Moreover the inspection of the individual errors of E_c parameter listed in Table 2 also reveal the presence of large and asymmetric errors for a significant fraction of the sample. Therefore the error estimation on the high energy cut-off presented should be treated cautiously. Instead, we choose to estimate the probability distribution of the cut-off values. We adopt a Markov chain Monte Carlo (MCMC) method in XSPEC, using the Goodman-Wearer algorithm, to derive the distribution of the E_c parameter for each accurately measured value. Then we calculate the average probability distribution of the actually measured high energy cut-offs by summing all the MCMC results of the individual sources.

In Fig. 7 we present the average probability distribution of the E_c parameter for the detections after taking into account the correct error distribution for each source using the MCMC simulation approach. The corrected distribution is slightly shifted to the right due to the uncertainties towards higher energies. The mean value of the observed E_c parameter, based on the MCMCs presented in Fig. 7 is 150 keV. The mean values of all spectral parameters are summarised in Table 3.

5. Simulations for the estimation of the true E_c distribution

The large number of upper limits in the spectral cut-off may cast some doubt on the validity of the values quoted above. The large number of upper limits can be partially attributed to the relatively limited bandwidth of the X-ray observations. Note that the value of the median (mean) cut-off is outside the *NuSTAR* spectral energy band-pass. In principle, the use of the survival analysis techniques alleviates this problem. However, an inherent assumption is that the upper limits originate from the same parent population with the actually constrained values. For example if there is a population with much higher coronal temperatures (cut-offs), or if our analysis systematically identifies only the low cut-off sources, this will not be imprinted on our results.

Moreover, a degeneracy between the photon index and the high-energy cut-off in the spectral model employed may affect the spectral fitting results (e.g. Tortosa et al. 2018). This degeneracy reflects the fact that an underestimated value of the E_c parameter can be compensated, in terms of goodness of fit, by a flatter photon index. Furthermore, imperfect modeling of the soft part of the X-ray spectrum may also induce correlations between the photon index and the high energy cut-off, particularly when observations from different instruments are combined (Molina et al. 2019) or alternatively when significant absorption is expected in the X-ray spectra (Baloković et al. 2020).

In order to determine the properties of the parent population, we employ detailed simulations taking into account all the possible observational degeneracies and systematics.

5.1. Description of the simulation methodology

Our idea is to simulate a number of spectral data sets with identical characteristics to those found for our sample, using however, each time, a different distribution only for the spectral cut-off E_c parameter. Then we repeat the same spectral analysis presented in section 3.2 to derive different output distributions for the high energy cut-off parameter. The goal is to identify the output E_c distribution, that best matches our observed sample distribution. Then the true distribution of our population would be the known, real distribution that corresponds to the best matched simulated sample.

We assume a skewed (Maxwell-Boltzmann) probability distribution for the spectral cut-off parameter:

$$f(x)dx = \sqrt{\frac{2}{\pi}} x^2 e^{-x^2/2\alpha} / \alpha^3 dx \quad (1)$$

This choice is motivated from the shape of the E_c distribution in Fig. 7. The distribution does not introduce unrealistic negative E_c values as would be the case if a Gaussian form was used. Moreover, this distribution presents the advantage that its shape is determined by only one parameter, the distribution parameter α , thus significantly reducing the number of the performed simulations. The distribution parameter α defines its mean value through the relation $\mu = 2\alpha \sqrt{2/\pi}$.

We also assume that the true distributions of the photon index and the reflection strength of our sample follow the derived observed distributions (see Fig. 5 and 6 respectively). This implicitly assumes that the spectral fitting does not affect the intrinsic distribution of the Γ and R parameters.

We simulate 14 samples assuming a different E_c distribution with the value of the distribution parameter α ranging from 25 keV to 500 keV. Each sample contains 10 times more sources

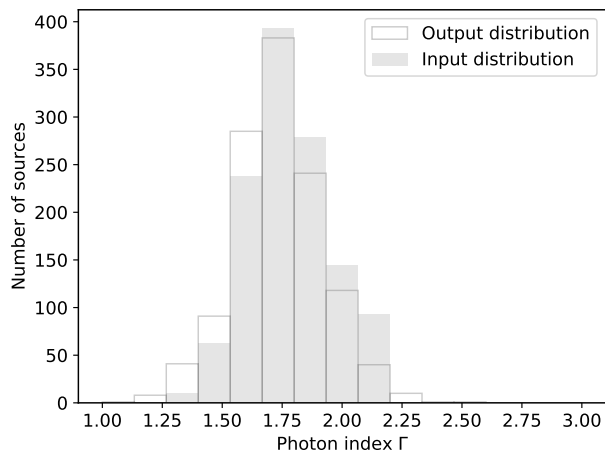


Fig. 8. Example of the comparison between the input and the output distributions of the photon index for a simulated sample with an α parameter of 175 keV.

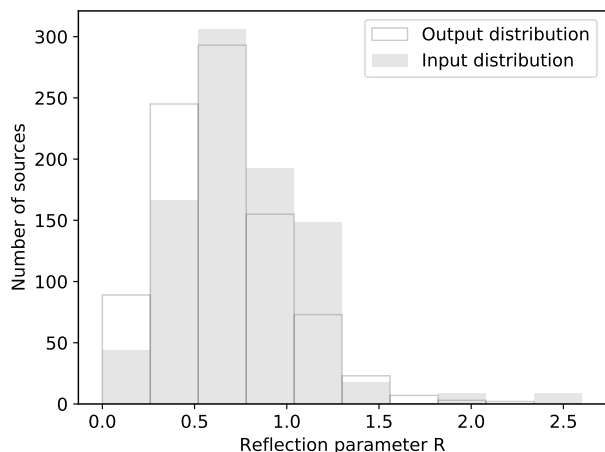


Fig. 9. Example of the comparison between the input and the output distributions of the reflection parameter for a simulated sample with an α parameter of 175 keV.

than our sample. Spectra and background files are created using XSPEC with the same count, Γ and R distributions with our sample. We fit the simulated data in each sample and try to measure the Γ , R and E_c parameters and their uncertainties at the 90 per cent confidence level in order to compare with the observations.

5.2. Simulation Results and comparison with the data

In all the simulations the photon index has been accurately constrained in 100 per cent of the spectral fits regardless of the assumed E_c distribution. The output distribution of the photon index, closely reproduces the input distribution in all cases. An example is presented in Fig. 8 where we plot the input and output Γ distributions for the simulated samples with an α parameter of 175 keV. The Kolmogorov-Smirnov test of the two distributions gives a probability of ~ 0.80 , supporting the hypothesis that the two distributions are equivalent.

Similarly, the output distribution of the reflection parameter closely follows the input distribution. In Fig. 9 we compare the input reflection's parameter distribution and the output one, i.e. after the spectral fitting, for the same simulated sample presented above. Again, there is a reasonable agreement suggesting that the observed R distribution represents the true R distribution of the sample. The Kolmogorov-Smirnov statistical comparison gives a probability of ~ 0.35 , absolutely consistent with our hypothesis. We note that both Γ and R distributions remains largely unaffected by the choice of the E_c parameter.

On the other hand the simulations reveal a quite different behaviour for the E_c parameter distribution. In Fig. 10 we compare the input (true) and the output (measured) distribution of the high energy cut-off, for the simulated samples, for an α parameter of 25, 50, 100, 150, 200 and 300 keV. Clearly, as we move towards higher α values the difference between the measured and the true distribution increases drastically. This behaviour is quantified in Fig. 11 where we plot the mean value of the input (true) distribution of E_c versus the mean value of the output (measured) distribution of E_c . We observe that when the mean E_c lies well within the *NuSTAR* pass-band, (i.e. significantly smaller than 80 keV) the output (measured) distribution is similar to the input (true) one. This is reasonable since in this case the data can provide reliable constraints on the spectral cut-off. As we move to higher mean energies, outside the *NuSTAR* pass-band, the input and the output mean E_c values diverge significantly.

In Fig. 12 we plot the expected fraction of E_c detections (at the 90 per cent confidence interval) versus the α parameter which characterize the input E_c distribution. The horizontal lines show the measured fraction of E_c detections in our sample (solid line) and its 90 per cent uncertainty (dashed lines). We see that the acceptable α solution should be found within 75 keV and 165 keV with the most probable value being at 125 keV. These results correspond to a true mean value for the E_c parameter of 200 ± 60 keV. For values outside this range, the observed fraction of sources with well measured E_c values (observational data) is inconsistent with the corresponding fraction obtained from the simulations. Furthermore, from Fig. 12 we can see that the fraction of securely inferred E_c values decreases with increasing E_c . This is also a reasonable result implying that higher E_c values are more difficult to be accurately measured in a given X-ray spectrum.

More stringent constraints can be placed through the comparison of the observed distribution presented in Fig. 7 with the normalized output distributions derived from the spectral fitting of the simulated samples (output distributions presented in Fig. 10). In Fig. 13 we compare our observed probability distribution with six different (output) distributions obtained from the simulations. These distributions correspond to an α parameter of 50, 75, 100, 125, 150 and 175 keV. A Kolmogorov-Smirnov test rejects the hypothesis that the distributions are the same for all but the $\alpha=100$ keV and $\alpha=125$ keV solutions. This suggest a true mean value for the E_c parameter of about 180 keV. This value is consistent, albeit somewhat lower, than that derived using the survival analysis (206 ± 38 keV). Our simulations are based on the assumption that the parent distribution follows a Maxwell Boltzmann distribution. However, the use of a similar symmetrical distribution could also provide acceptable results. For example a Gaussian distribution with mean of 200 keV and $\sigma=80$ keV, can also reproduce our observations. This is reasonable since this distribution is similar to a Maxwell-Boltzmann distribution with $\alpha=125$ keV.

Combining this result with our estimates on the mean photon index and the mean high energy cut-off, we can estimate the

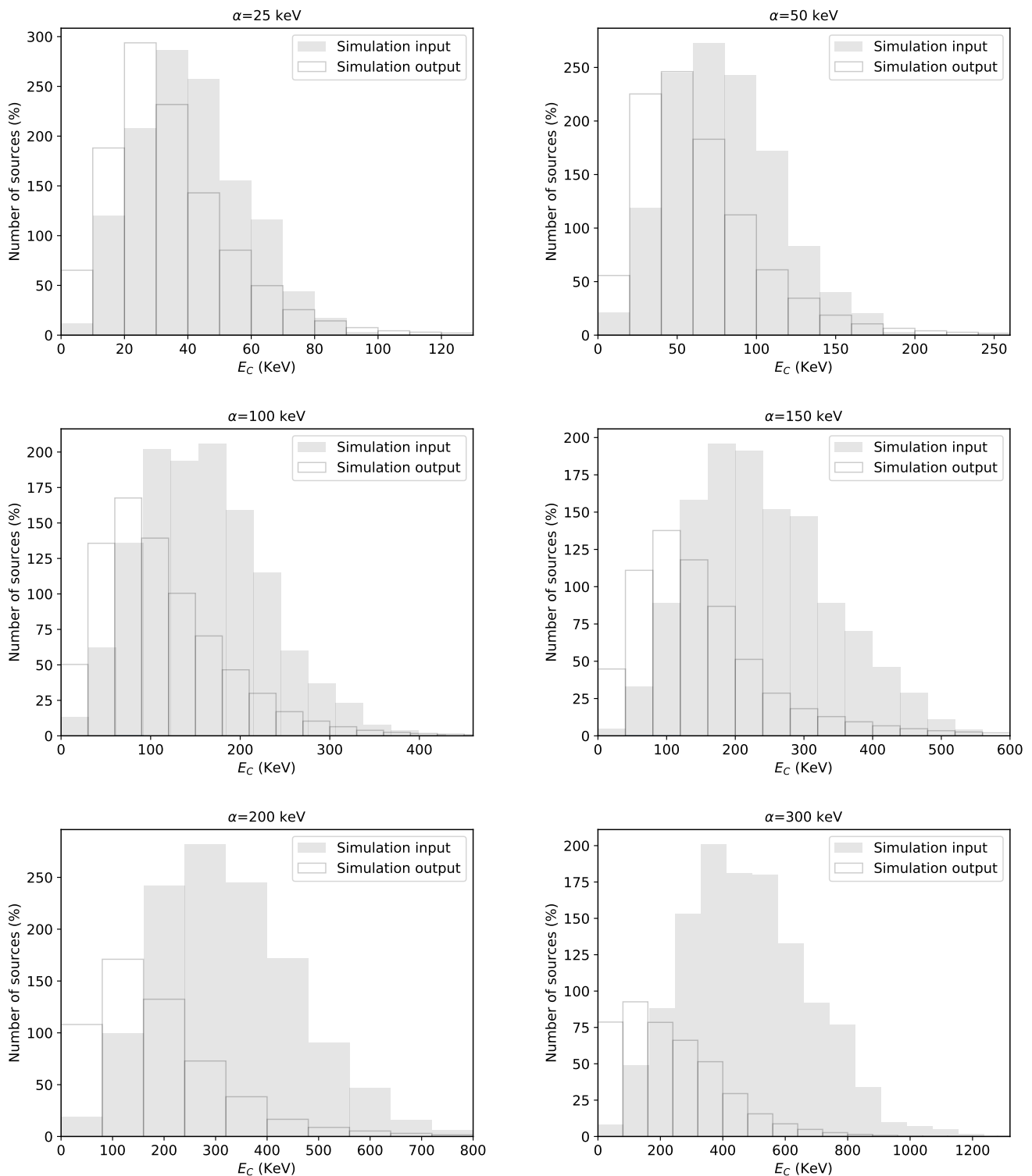


Fig. 10. Comparison between the input and the output distributions of the high energy cut-off parameter for a six simulated sample with an α parameter of 25, 50, 100, 150, 200, and 300 keV.

mean properties of the corona for the Seyfert 1 population. Following Petrucci et al. (2001) the mean optical depth is approximately $\tau_e = 1.82 \pm 0.14$ and the mean temperature approximately $kT_e = 65 \pm 10$ keV.

6. Summary and conclusions

We present the analysis of the *NuSTAR* spectra (3-80 keV) of a sample of 118 Seyfert 1 galaxies selected from the BAT all sky survey 105-month catalogue. This is the largest sample of Seyfert 1 galaxies with *NuSTAR* spectra presented in the literature. Our main goal is to constrain the cut-off energy of the

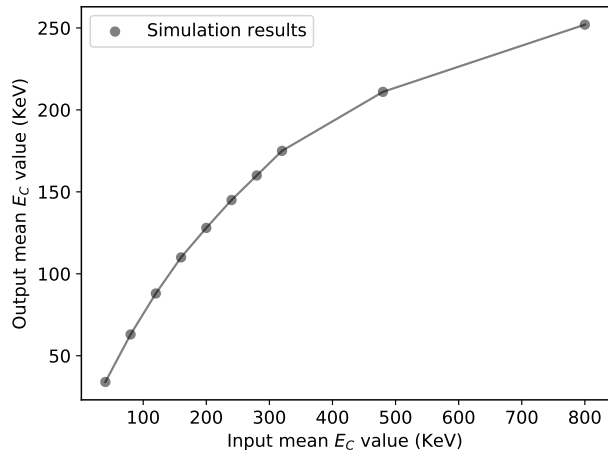


Fig. 11. The mean value of the spectral cut-off E_c of the input distribution of E_c versus the output distribution.

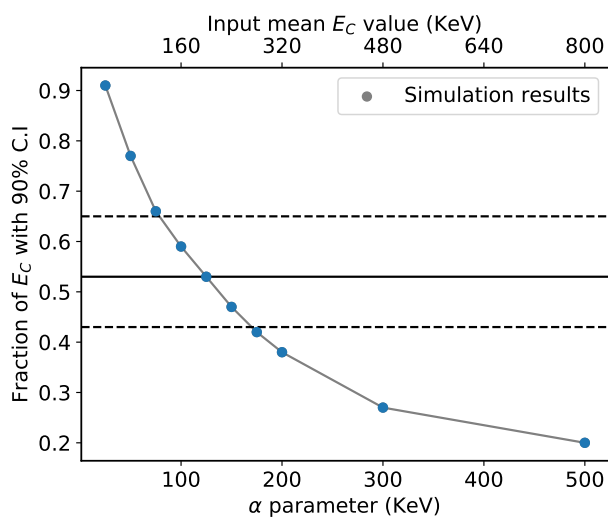


Fig. 12. The fraction of sources with E_c securely inferred values (not censored) as a function of the value of the α parameter. The solid horizontal line defines the fraction of E_c securely inferred measurements (no censored values) while the horizontal dashed lines denote the 90 per cent uncertainty.

power-law spectrum and hence the temperature of the hot corona that produces the X-ray emission. Our results can be summarised as follows.

We find secure estimates for the spectral cut-off in 62 sources (53% of our sample) while for the remaining sources only lower limits could be derived. The median (mean) value for the well constrained sources is 89 (103) keV with the distribution being highly skewed towards higher energies; the 25 and 75% quartiles are 65 and 102 keV respectively. As the exclusion of the lower limits bias our sample towards the detection of the low energy spectral cut-offs, we estimate the spectral cut-off for the full sample using survival analysis techniques. The true mean value increases to 206 ± 38 keV. Furthermore, we check the validity of our results by performing extensive spectral simulations. This is important since the derived spectral cut-off lies outside the *NuSTAR* spectral pass-band (3–80 keV) and this could impede the

accurate estimation of the spectral cut-off. Under the assumption of an underlying Maxwell-Boltzmann distribution, our simulations suggest that the spectral cut-off of the parent population is $E_c \approx 160 - 200$ keV significantly higher than that inferred from the actual observations. This is comparable with the value derived using survival analysis techniques.

Our work also provides strong constraints on other spectral parameters. The mean value of the photon index is $\Gamma = 1.78 \pm 0.01$. This is in good agreement with previous estimates of BAT selected Seyfert 1 galaxy spectra which have been fitted using a combination of BAT and softer X-ray spectra from *Chandra XMM - Newton* and *Gehrels Swift /XRT*. Also the reflection parameter derived from the full sample has a mean value of $R = 0.69 \pm 0.04$. Again this is in reasonable agreement with the previous BAT results on Seyfert 1 galaxies but the excellent quality of the *NuSTAR* spectra reduced significantly the fraction of censored values thus providing much more stringent constraints.

Combining these results, our work provides stringent constraints on the mean properties of the corona. The mean optical depth is approximately 1.82 ± 0.14 and the mean temperature approximately 65 ± 10 keV.

Acknowledgements. We have made use of data from the *NuSTAR* mission, a project led by the California Institute of Technology, managed by the Jet Propulsion Laboratory, and funded by the National Aeronautics and Space Administration. We thank the *NuSTAR* Operations, Software and Calibration teams for support with the execution and analysis of these observations. This research has made use of the *NuSTAR* Data Analysis Software (NuSTARDAS) jointly developed by the Space Science Data Center (SSDC; ASI, Italy) and the California Institute of Technology (USA). This work is based on archival data, software or online services provided by the SSDC. This research has made use of the High Energy Astrophysics Science Archive Research Center Online Service, provided by the NASA/Goddard Space Flight Center and NASA's Astrophysics Data System.

References

- Arnaud, K. A. 1996, in *Astronomical Society of the Pacific Conference Series*, Vol. 101, *Astronomical Data Analysis Software and Systems V*, ed. G. H. Jacoby & J. Barnes, 17
- Baloković, M., Harrison, F. A., Madejski, G., et al. 2020, *ApJ*, 905, 41
- Barthelmy, S. D. 2004, in *Society of Photo-Optical Instrumentation Engineers (SPIE) Conference Series*, Vol. 5165, *X-Ray and Gamma-Ray Instrumentation for Astronomy XIII*, ed. K. A. Flanagan & O. H. W. Siegmund, 175–189
- Baumgartner, W. H., Tueller, J., Markwardt, C. B., et al. 2013, *ApJS*, 207, 19
- Brandt, W. N. & Alexander, D. M. 2015, *A&A Rev.*, 23, 1
- Chartas, G., Rhea, C., Kochanek, C., et al. 2016, *Astronomische Nachrichten*, 337, 356
- Dadina, M. 2007, *A&A*, 461, 1209
- Emmanoulopoulos, D., Papadakis, I. E., Dovčiak, M., & McHardy, I. M. 2014, *MNRAS*, 439, 3931
- Fabian, A. C., Lohfink, A., Kara, E., et al. 2015, *MNRAS*, 451, 4375
- Gehrels, N., Chincarini, G., Giommi, P., et al. 2004, *ApJ*, 611, 1005
- Guerras, E., Dai, X., Steele, S., et al. 2017, *ApJ*, 836, 206
- Haardt, F. & Maraschi, L. 1991, *ApJ*, 380, L51
- Harrison, F. A., Craig, W. W., Christensen, F. E., et al. 2013, *ApJ*, 770, 103
- Isobe, T., Feigelson, E. D., & Nelson, P. I. 1986, *ApJ*, 306, 490
- Johnson, W. N., McNaron-Brown, K., Kurfess, J. D., et al. 1997, *ApJ*, 482, 173
- Kallman, T. & Bautista, M. 2001, *ApJS*, 133, 221
- Kamraj, N., Harrison, F. A., Baloković, M., Lohfink, A., & Brightman, M. 2018, *ApJ*, 866, 124
- Kara, E., Alston, W. N., Fabian, A. C., et al. 2016, *MNRAS*, 462, 511
- Ludlam, R. M., Cackett, E. M., Gültekin, K., et al. 2015, *MNRAS*, 447, 2112
- Malizia, A., Molina, M., Bassani, L., et al. 2014, *ApJ*, 782, L25
- Matt, G., Baloković, M., Marinucci, A., et al. 2015, *MNRAS*, 447, 3029
- Matt, G., Bianchi, S., Guainazzi, M., et al. 2011, *A&A*, 533, A1
- McHardy, I. M., Gunn, K. F., Uttley, P., & Goad, M. R. 2005, *MNRAS*, 359, 1469
- Molina, M., Malizia, A., Bassani, L., et al. 2019, *MNRAS*, 484, 2735
- Nandra, K., O'Neill, P., George, I., & Reeves, J. 2007, *Monthly Notices of the Royal Astronomical Society*, 382
- Oh, K., Koss, M., Markwardt, C. B., et al. 2018, *ApJS*, 235, 4

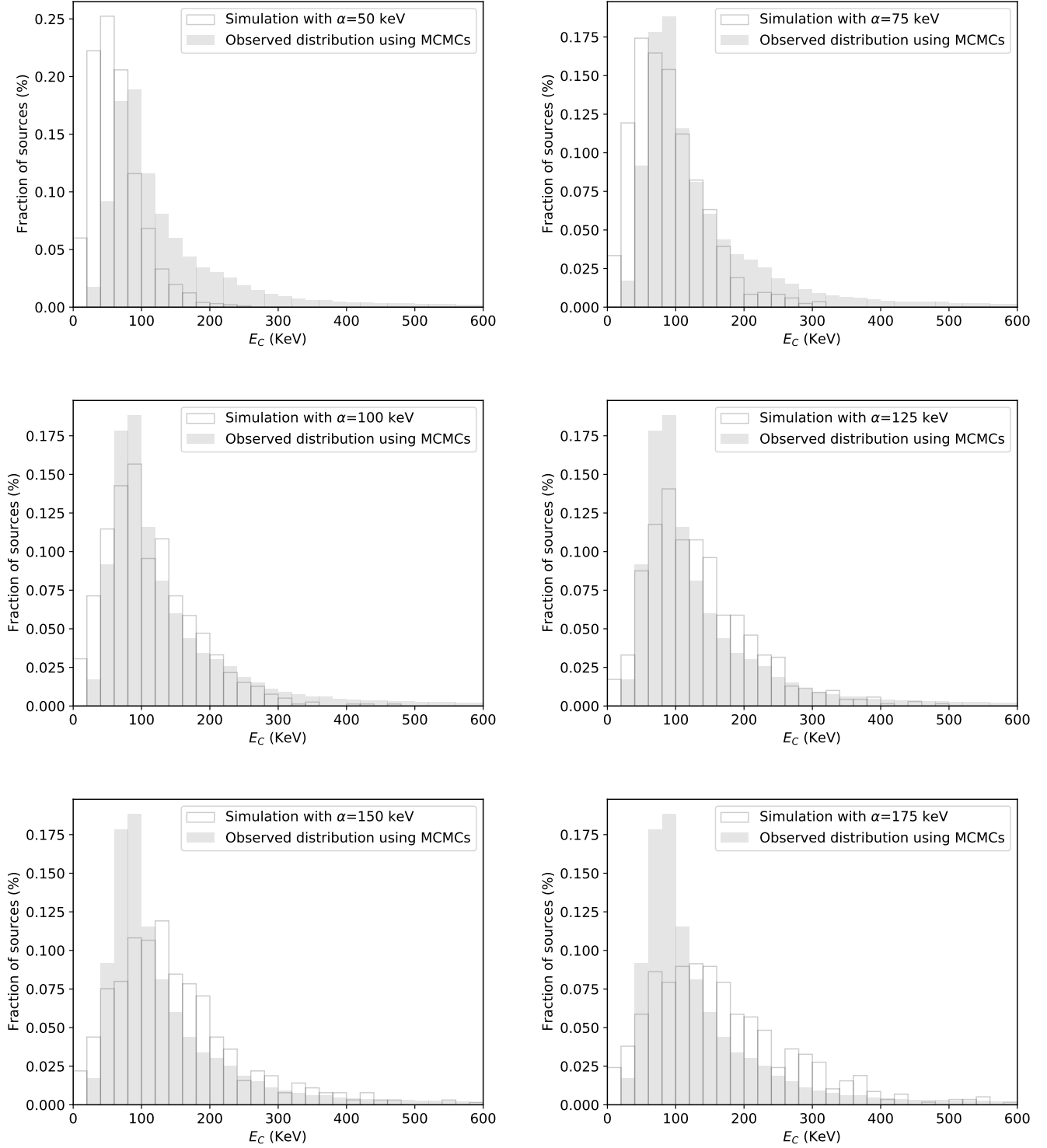


Fig. 13. Comparison between the observed distribution and the output distributions of the high energy cut-off parameter for a six different simulated samples with an α parameter of 50, 75, 100, 125, 150 and 175 keV.

Table 3. Mean values for the spectral parameters

	Direct estimates	Survival analysis
Photon Index	1.78 ± 0.01 (118/118)	-
Reflection	0.68 ± 0.05 (106/118)	0.69 ± 0.04
Cut-off energy	102 ± 16 keV (63/118)	206 ± 38

Notes: As the cut-off energy distribution is highly skewed, often presenting large asymmetric error-bars the error approximation is unrealistic.

- Perri, M., Puccetti, S., & N., S. 2017, The NuSTAR Data Analysis Software Guide v1.9.3
- Petrucci, P. O., Merloni, A., Fabian, A., Haardt, F., & Gallo, E. 2001, *MNRAS*, 328, 501
- Rani, P., Stalin, C. S., & Goswami, K. D. 2019, *MNRAS*, 484, 5113
- Reeves, J., Done, C., Pounds, K., et al. 2008, *MNRAS*, 385, L108
- Ricci, C., Trakhtenbrot, B., Koss, M. J., et al. 2017, *ApJS*, 233, 17
- Tortosa, A., Bianchi, S., Marinucci, A., Matt, G., & Petrucci, P. O. 2018, *A&A*, 614, A37
- Uttley, P., Cackett, E. M., Fabian, A. C., Kara, E., & Wilkins, D. R. 2014, *A&A Rev.*, 22, 72
- Vaiana, G. S. & Rosner, R. 1978, *ARA&A*, 16, 393

Table 1. Log of the *NuSTAR* observations of Seyfert 1 galaxies

BAT obsID	Name	<i>NuSTAR</i> obsID	Redshift	Net counts	Type
6	Mrk335	60001041005	0.025	26434	Sy1.2
19	2MASXJ00341665-7905204	60160015002	0.074	6353	Sy1.0
36	Mrk1148	60160028002	0.064	18300	Sy1.5
73	Fairall9	60001130003	0.047	84991	Sy1.2
77	Mrk359	60402021002	0.017	12822	Sy1.5
78	MCG-03-04-072	60160061002	0.046	9359	Sy1.0
98	1ES0152+022	60160080002	0.082	6202	Sy1.0
106	Mrk1018	60301022003	0.042	2853	Sy1.2
116	Mrk590	90201043002	0.026	7078	Sy1.5
117	2MASXJ02143730-6430052	60061021002	0.074	5131	Sy1.0
127	AM0224-283	60363002002	0.059	3060	Sy1.2
129	NGC931	60101002004	0.016	72618	Sy1.5
130	Mrk1044	60160109002	0.016	8144	Sy1.0
134	NGC985	60061025002	0.043	7232	Sy1.5
147	HB890241+622	60160125002	0.044	24951	Sy1.2
175	LCRSB032315.2-420449	60160152002	0.058	2766	Sy1.0
191	HE0345-3033	60376003002	0.095	895	Sy1.0
214	3C111.0	60202061006	0.048	62073	Sy1.2
216	NGC1566	80401601002	0.005	56882	Sy1.5
220	1H0419-577	60101039002	0.104	109546	Sy1.5
224	2MASXJ04293830-2109441	60260006002	0.070	1645	Sy1.2
229	2MASXJ04372814-4711298	60160197002	0.053	3913	Sy1.0
234	IRAS04392-2713	60160201002	0.083	5809	Sy1.5
266	Ark120	60001044004	0.032	107956	Sy1.0
269	ESO362-18	60201046002	0.012	51569	Sy1.5
310	MCG+08-11-011	60201027002	0.021	219306	Sy1.5
314	PKS0558-504	60160254002	0.137	7443	Sy1.0
328	NVSSJ062335+644538	60376012002	0.086	4895	Sy1.0
376	1RXSJ073308.7+455511	60260007002	0.141	2310	Sy1.0
378	Mrk9	60061326002	0.039	3189	Sy1.2
402	ESO209-G012	60160315002	0.040	11223	Sy1.5
409	PG0804+761	60160322002	0.100	5241	Sy1.0
423	Fairall1146	60061082002	0.031	11993	Sy1.5
425	3C206	60160332002	0.197	7941	Sy1.0
431	1RXSJ084521.7-353048	60061085002	0.137	2311	Sy1.0
447	IRAS09149-6206	90401630002	0.057	67745	Sy1.0
449	Mrk704	60061090002	0.029	9936	Sy1.2
455	MCG+04-22-042	60061092002	0.032	17273	Sy1.2
458	Mrk110	60201025002	0.035	292836	Sy1.5
473	3C227	60061329002	0.085	8066	Sy1.2
485	ESO374-G025	60160384002	0.023	1556	Sy1.0
495	2MASXJ10195855-0234363	60260015002	0.060	550	Sy1.0
497	NGC3227	60202002002	0.003	83393	Sy1.5
512	SDSSJ104326.47+110524.2	60376004002	0.047	6699	Sy1.5
524	Mrk728	60061338002	0.035	4050	Sy1.5
530	NGC3516	60002042004	0.008	20304	Sy1.2
532	IC2637	60061208002	0.029	9471	Sy1.5
542	ARP151	60160430002	0.021	2410	Sy1.2
552	Mrk739E	60260008002	0.029	3416	Sy1.0
556	SBS1136+594	60160443002	0.060	10380	Sy1.5
558	NGC3783	60101110004	0.009	70805	Sy1.2
565	KUG1141+371	60160449002	0.038	7438	Sy1.2
566	UGC06728	60376007002	0.006	34838	Sy1.2
567	2MASXJ11454045-1827149	60302002006	0.032	26050	Sy1.2
574	2MASXJ11491868-0416512	60061215002	0.084	5928	Sy1.0
576	PG1149-110	60160458002	0.049	1227	Sy1.2
583	Mrk1310	60160465002	0.019	7840	Sy1.5
585	NGC4051	60401009002	0.002	217209	Sy1.5
587	GQCom	60160469002	0.165	4610	Sy1.5
589	2MASXJ12055599+4959561	60061357002	0.063	1666	Sy1.5

Table 1. continued.

BAT obsID	Name	<i>NuSTAR</i> obsID	Redshift	Net counts	Type
608	Mrk766	60001048002	0.013	74065	Sy1.5
611	Mrk205	60160490002	0.071	7215	Sy1.0
623	Mrk771	60061229002	0.063	3368	Sy1.2
631	NGC4593	60001149002	0.009	23920	Sy1.0
636	WKK1263	60160510002	0.024	21298	Sy1.5
644	6dFJ1254564-265702	60363001002	0.059	4877	Sy1.2
686	NGC5273	60061350002	0.003	16637	Sy1.5
690	2MASSJ1346085+732053	60160556002	0.290	2194	Sy1.0
694	IC4329A	60001045002	0.016	697782	Sy1.5
695	UM614	60160560002	0.032	5760	Sy1.5
697	Mrk279	60160562002	0.03	27192	Sy1.5
717	NGC5548	60002044006	0.017	85416	Sy1.5
726	Mrk813	60160583002	0.110	8088	Sy1.2
728	Mrk1383	60061254002	0.086	10981	Sy1.0
730	Mrk684	60160586002	0.046	2867	Sy1.0
735	Mrk817	60160590002	0.031	7459	Sy1.2
741	IGRJ14471-6414	60061257002	0.053	2608	Sy1.0
750	WKK4438	60401022002	0.016	35926	Sy1.5
753	Mrk841	60101023002	0.036	16341	Sy1.2
754	Mrk1392	60160605002	0.036	4818	Sy1.5
765	2MASXJ15144217-8123377	60061263002	0.068	2820	Sy1.2
774	Mrk290	60061266004	0.029	8903	Sy1.5
794	LEDA100168	60160631002	0.183	3360	Sy1.0
795	WKK6092	60160632002	0.015	9800	Sy1.5
810	VII Zw653	60160639002	0.063	6125	Sy1.2
815	Mrk885	60160641002	0.025	3725	Sy1.0
833	2MASXJ16481523-3035037	60160648002	0.031	1956	Sy1.0
888	2MASXJ17311341+1442561	60161666002	0.082	2124	Sy1.0
905	2E1739.1-1210	60160670002	0.037	10453	Sy1.0
907	4C+18.51	60160672002	0.186	2980	Sy1.0
912	1RXSJ174538.1+290823	60160674002	0.110	6256	Sy1.5
924	Mrk507	60160675002	0.056	810	Sy1.2
925	VII Zw742	60160676002	0.063	1881	Sy1.2
948	2MASXJ1802473-145454	60160680002	0.036	17794	Sy1.2
967	H1821+643	60160683002	0.297	13180	Sy1.2
976	1RXSJ182557.5-071021	60160688002	0.037	1076	Sy1.0
984	3C382	60001084002	0.058	102343	Sy1.2
994	3C390.3	60001082003	0.056	81788	Sy1.5
1013	2MASXJ18560128+1538059	60160701002	0.084	7696	Sy1.2
1021	CGCG229-015	60160705002	0.028	4594	Sy1.0
1032	ESO141-G055	60201042002	0.036	97395	Sy1.2
1041	2MASSJ19334715+3254259	60160714002	0.058	7752	Sy1.2
1042	2MASXJ19373299-0613046	60101003002	0.010	54586	Sy1.5
1043	2MASXJ19380437-5109497	60160716002	0.040	7531	Sy1.2
1046	NGC6814	60201028002	0.005	215189	Sy1.5
1082	4C+21.55	60160740002	0.173	7435	Sy1.0
1084	2MASXJ20350566+2603301	60160741002	0.048	2017	Sy1.5
1088	4C+74.26	60001080006	0.104	106864	Sy1.0
1090	Mrk509	60101043002	0.034	323647	Sy1.2
1106	2MASXJ21192912+3332566	60061358002	0.051	8248	Sy1.5
1111	SWIFTJ212745.6+565636	60001110005	0.014	95594	Sy1.0
1117	2MASXJ21355399+4728217	60160761002	0.025	7267	Sy1.5
1125	RXJ2145.5+1102	60160767002	0.209	2093	Sy1.0
1162	MCG+01.57-016	60061343002	0.025	4026	Sy1.5
1172	MR2251-178	60102025004	0.064	52719	Sy1.2
1182	NGC7469	60101001008	0.016	28817	Sy1.5
1381	PG1100+772	60463031002	0.311	3196	Sy1.0
1471	Mrk871	60361014002	0.033	4931	Sy1.0
1503	Mrk506	60464138002	0.043	3421	Sy1.5
1536	2MASSJ1830231+731310	60464150002	0.123	6803	Sy1.0
1581	3C410	60463069002	0.248	2236	Sy1.5

Table 1. continued.

BAT obsID	Name	<i>NuSTAR</i> obsID	Redshift	Net counts	Type
1611	ESO344-G016	60361017002	0.039	9766	Sy1.5

Table 2. Log of the *NuSTAR* observations of Seyfert 1 galaxies

BAT obsID	Γ ^(a)	R ^(a)	E_c ^(b)	$F_{2-10 \text{ keV}}$ ^(c)	$L_{2-10 \text{ keV}}$ ^(d)	$F_{20-40 \text{ keV}}$ ^(c)	$L_{20-40 \text{ keV}}$ ^(d)	χ^2/dof	error id ^(e)
6	2.02 ^{+0.05} _{-0.06}	1.90 ^{+0.34} _{-0.31}	>365	0.65	0.1	0.53	0.08	795 / 715	0
19	2.03 ^{+0.14} _{-0.14}	1.29 ^{+0.64} _{-0.56}	60 ⁺⁷⁷ ₋₂₃	0.78	1.05	0.31	0.43	259 / 259	1
36	1.78 ^{+0.07} _{-0.07}	0.14 ^{+0.18} _{-0.13}	87 ⁺⁷⁶ ₋₂₈	2.05	2.01	1.04	1.04	575 / 547	1
73	1.94 ^{+0.03} _{-0.03}	0.85 ^{+0.12} _{-0.12}	196 ⁺¹¹² ₋₅₄	2.45	1.28	1.38	0.72	1014 / 1051	1
77*	1.87 ^{+0.08} _{-0.08}	0.89 ^{+0.32} _{-0.28}	>118	0.61	0.04	0.41	0.03	492 / 481	0
78	1.82 ^{+0.09} _{-0.09}	0.68 ^{+0.34} _{-0.29}	102 ⁺¹⁶⁹ ₋₄₂	1.08	0.53	0.66	0.33	358 / 362	1
98*	1.75 ^{+0.11} _{-0.12}	0.34 ^{+0.38} _{-0.21}	>84	0.68	1.11	0.46	0.77	277 / 259	0
106*	1.85 ^{+0.22} _{-0.21}	0.85 ^{+0.76} _{-0.58}	>47	0.17	0.07	0.1	0.04	152 / 152	0
116	1.71 ^{+0.13} _{-0.13}	1.16 ^{+0.5} _{-0.42}	66 ⁺⁸⁶ ₋₂₆	0.32	0.05	0.24	0.04	313 / 307	1
117	1.69 ^{+0.13} _{-0.09}	<0.34	99 ⁺²³⁵ ₋₅₃	0.54	0.72	0.32	0.42	211 / 219	1
127	1.81 ^{+0.14} _{-0.17}	0.83 ^{+0.72} _{-0.54}	>80	0.31	0.26	0.27	0.23	127 / 148	0
129	1.83 ^{+0.03} _{-0.03}	0.71 ^{+0.12} _{-0.11}	172 ⁺¹⁰⁸ ₋₅₀	2.92	0.18	1.89	0.12	1027 / 1061	1
130	2.12 ^{+0.09} _{-0.11}	1.13 ^{+0.54} _{-0.43}	>120	0.85	0.05	0.46	0.03	414 / 414	0
134	1.49 ^{+0.11} _{-0.11}	0.60 ^{+0.34} _{-0.33}	49 ⁺³³ ₋₁₅	1.2	0.52	0.83	0.36	385 / 380	1
147	1.7 ^{+0.05} _{-0.05}	0.74 ^{+0.2} _{-0.18}	144 ⁺¹¹³ ₋₄₆	2.53	1.14	2.08	0.94	667 / 679	1
175*	1.77 ^{+0.19} _{-0.21}	0.72 ^{+0.73} _{-0.58}	>52	0.3	0.24	0.2	0.16	134 / 134	0
191	1.82 ^{+0.71} _{-0.41}	<0.48	>16	0.05	0.11	0.02	0.05	59 / 75	0
214	1.66 ^{+0.03} _{-0.03}	<0.2	148 ⁺¹⁰² ₋₄₃	3.14	1.72	2.09	1.15	958 / 948	1
216	1.76 ^{+0.03} _{-0.03}	0.75 ^{+0.13} _{-0.13}	336 ⁺⁶⁴⁶ ₋₁₄₀	1.84	0.01	1.54	0.01	991 / 961	1
220	1.64 ^{+0.03} _{-0.03}	0.26 ^{+0.07} _{-0.07}	52 ⁺⁴ ₋₄	1.56	4.2	0.92	2.59	1121 / 1138	1
224	1.70 ^{+0.34} _{-0.32}	2.47 ^{+2.13} _{-1.22}	48 ⁺²²¹ ₋₂₄	0.15	0.18	0.13	0.17	83 / 88	1
229	2.10 ^{+0.11} _{-0.12}	0.88 ^{+0.75} _{-0.32}	>142	0.49	0.33	0.26	0.18	197 / 177	0
234	1.77 ^{+0.13} _{-0.13}	0.47 ^{+0.38} _{-0.32}	64 ⁺⁹⁷ ₋₂₆	0.74	1.27	0.4	0.7	244 / 248	1
266	1.97 ^{+0.03} _{-0.03}	0.78 ^{+0.11} _{-0.11}	233 ⁺¹⁴⁷ ₋₆₇	4.45	1.07	2.43	0.58	1312 / 1105	1
269	1.58 ^{+0.04} _{-0.04}	0.95 ^{+0.15} _{-0.14}	77 ⁺¹⁸ ₋₁₃	1.16	0.04	1.08	0.04	956 / 962	1
310	1.82 ^{+0.02} _{-0.02}	0.53 ^{+0.06} _{-0.06}	140 ⁺²⁹ ₋₂₁	5.83	0.55	3.57	0.34	1588 / 1438	1
314	2.19 ^{+0.07} _{-0.06}	<0.39	>88	1.04	5.4	0.32	1.67	232 / 293	0
328	1.77 ^{+0.11} _{-0.11}	<0.35	>109	0.25	0.45	0.16	0.3	198 / 230	0
376*	1.63 ^{+0.21} _{-0.23}	<0.72	>38	0.24	1.22	0.15	0.82	107 / 113	0
378	1.81 ^{+0.12} _{-0.12}	1.05 ^{+0.72} _{-0.28}	>257	0.29	0.11	0.3	0.11	166 / 153	0
402	1.94 ^{+0.06} _{-0.08}	0.56 ^{+0.31} _{-0.25}	>159	1.3	0.5	0.74	0.28	420 / 427	0
409	1.92 ^{+0.1} _{-0.11}	0.88 ^{+0.56} _{-0.45}	>182	0.7	1.77	0.53	1.33	176 / 221	0
423	1.90 ^{+0.08} _{-0.08}	0.94 ^{+0.34} _{-0.31}	127 ⁺²⁴⁶ ₋₅₄	1.48	0.34	0.87	0.2	465 / 439	1
425*	1.78 ^{+0.11} _{-0.11}	0.31 ^{+0.37} _{-0.28}	>79	1.11	12.04	0.67	7.53	285 / 322	0
431	1.47 ^{+0.18} _{-0.03}	<0.51	102 ⁺¹⁸¹ ₋₆₇	0.49	2.39	0.37	1.77	93 / 110	1
447	1.81 ^{+0.03} _{-0.03}	0.85 ^{+0.12} _{-0.12}	96 ⁺²⁴ ₋₁₆	1.5	1.17	1.0	0.79	1163 / 994	1
455	1.92 ^{+0.06} _{-0.06}	0.53 ^{+0.24} _{-0.22}	>153	2.36	0.57	1.35	0.32	495 / 535	0
458	1.74 ^{+0.02} _{-0.02}	0.17 ^{+0.04} _{-0.04}	93 ⁺¹³ ₋₁₀	4.02	1.15	2.27	0.66	1619 / 1539	1
473	1.57 ^{+0.10} _{-0.04}	<0.25	74 ⁺²² ₋₂₉	1.37	2.49	0.8	1.46	302 / 315	1
485	1.49 ^{+0.30} _{-0.08}	<0.47	>21	0.18	0.02	0.12	0.01	97 / 83	0
495	1.52 ^{+0.70} _{-0.25}	<0.85	>11	0.06	0.05	0.03	0.02	53 / 41	0
497	1.62 ^{+0.03} _{-0.03}	0.71 ^{+0.10} _{-0.10}	94 ⁺¹⁹ ₋₁₄	3.91	0.01	3.41	0.01	1186 / 1112	1
512	1.71 ^{+0.11} _{-0.12}	0.34 ^{+0.36} _{-0.31}	90 ⁺⁶⁴⁰ ₋₄₄	0.54	0.29	0.34	0.18	282 / 275	1
524	1.53 ^{+0.15} _{-0.16}	0.49 ^{+0.48} _{-0.4}	58 ⁺¹³⁰ ₋₂₆	0.44	0.13	0.32	0.09	175 / 187	1
530	1.60 ^{+0.07} _{-0.07}	1.29 ^{+0.29} _{-0.26}	89 ⁺⁴⁸ ₋₂₄	0.71	0.01	0.65	0.01	684 / 656	1
532	1.80 ^{+0.07} _{-0.09}	0.32 ^{+0.31} _{-0.25}	>105	0.85	0.16	0.58	0.11	342 / 371	0
542	1.74 ^{+0.19} _{-0.21}	1.01 ^{+0.98} _{-0.72}	>48	0.24	0.02	0.21	0.02	128 / 120	0
552	2.03 ^{+0.12} _{-0.11}	1.03 ^{+0.74} _{-0.62}	>270	0.45	0.09	0.29	0.06	168 / 159	0
556	1.71 ^{+0.09} _{-0.09}	0.47 ^{+0.29} _{-0.26}	75 ⁺⁶⁸ ₋₂₅	1.04	0.89	0.68	0.59	371 / 405	1
558	1.56 ^{+0.03} _{-0.03}	1.05 ^{+0.13} _{-0.12}	76 ⁺¹² ₋₁₀	3.91	0.08	3.74	0.08	1148 / 1088	1
565	1.75 ^{+0.1} _{-0.10}	0.34 ^{+0.34} _{-0.29}	>79	0.86	0.29	0.6	0.2	293 / 300	0
566	1.70 ^{+0.04} _{-0.04}	0.48 ^{+0.14} _{-0.14}	152 ⁺¹³¹ ₋₅₀	1.37	0.01	1.09	0.01	765 / 786	1
567	1.81 ^{+0.05} _{-0.05}	0.46 ^{+0.17} _{-0.16}	92 ⁺⁴⁸ ₋₂₅	2.73	0.68	1.66	0.42	586 / 646	1
574	1.98 ^{+0.14} _{-0.14}	1.17 ^{+0.66} _{-0.51}	>72	0.36	0.63	0.23	0.41	275 / 280	0
576*	1.65 ^{+0.36} _{-0.37}	1.49 ^{+1.77} _{-0.32}	>27	0.19	0.11	0.14	0.08	49 / 66	0
583	1.76 ^{+0.09} _{-0.10}	0.33 ^{+0.32} _{-0.28}	>81	0.9	0.08	0.6	0.05	281 / 313	0

Table 2. continued.

BAT obsID	Γ^a	R^a	$E_c^b(\text{keV})$	$F_{2-10 \text{ keV}}^a$	$L_{2-10 \text{ keV}}^b$	$F_{20-40 \text{ keV}}^a$	$L_{20-40 \text{ keV}}^b$	χ^2/dof	error id ^(e)
585	1.92 ^{+0.02} _{-0.02}	1.1 ^{+0.08} _{-0.07}	>846	1.71	0.0	1.37	0.0	1677 / 1577	0
587	1.61 ^{+0.14} _{-0.15}	<0.62	73 ⁺³¹⁹ ₋₃₅	0.38	2.79	0.25	1.87	167 / 214	1
589	1.86 ^{+0.19} _{-0.25}	1.13 ^{+1.14} _{-0.81}	>54	0.17	0.16	0.14	0.14	79 / 88	0
608	2.09 ^{+0.03} _{-0.03}	0.71 ^{+0.13} _{-0.12}	242 ⁺²⁹² ₋₈₈	2.4	0.09	1.01	0.04	1054 / 925	1
611	1.92 ^{+0.08} _{-0.11}	0.37 ^{+0.39} _{-0.3}	>108	0.92	1.12	0.51	0.62	268 / 289	0
623	2.07 ^{+0.15} _{-0.17}	1.29 ^{+1.03} _{-0.68}	>81	0.42	0.4	0.24	0.23	147 / 158	0
631*	1.85 ^{+0.05} _{-0.05}	0.79 ^{+0.22} _{-0.2}	>218	2.47	0.04	1.81	0.03	637 / 644	0
636	1.77 ^{+0.04} _{-0.06}	0.19 ^{+0.17} _{-0.14}	>282	3.12	0.42	2.1	0.28	329 / 304	0
644	1.55 ^{+0.13} _{-0.09}	<0.39	91 ⁺¹⁰⁰ ₋₅₀	0.61	0.5	0.42	0.34	182 / 221	1
686	1.59 ^{+0.07} _{-0.07}	0.74 ^{+0.24} _{-0.22}	115 ⁺⁹¹ ₋₃₇	2.0	0.01	1.82	0.0	631 / 569	1
690	2.00 ^{+0.22} _{-0.24}	1.13 ^{+1.55} _{-0.85}	>70	0.3	7.7	0.2	5.41	100 / 107	0
694	1.71 ^{+0.01} _{-0.12}	0.43 ^{+0.03} _{-0.03}	132 ⁺¹² ₋₁₀	11.3	0.65	8.42	0.48	2267 / 2014	1
695	1.61 ^{+0.12} _{-0.12}	0.53 ^{+0.38} _{-0.32}	88 ⁺¹⁸⁷ ₋₃₈	0.75	0.18	0.59	0.15	235 / 243	1
697	1.97 ^{+0.05} _{-0.05}	0.54 ^{+0.21} _{-0.19}	>163	2.66	0.56	1.41	0.3	700 / 643	0
717	1.54 ^{+0.03} _{-0.03}	0.59 ^{+0.09} _{-0.09}	63 ⁺⁹ ₋₇	4.22	0.28	3.36	0.22	1193 / 1091	1
726	2.01 ^{+0.08} _{-0.09}	0.77 ^{+0.41} _{-0.34}	>215	0.81	2.54	0.48	1.51	328 / 326	0
728	2.06 ^{+0.09} _{-0.09}	1.28 ^{+0.48} _{-0.39}	>151	0.85	1.58	0.53	0.98	369 / 419	0
730	2.15 ^{+0.16} _{-0.19}	1.52 ^{+1.29} _{-0.81}	>73	0.36	0.18	0.2	0.1	131 / 135	0
735*	1.73 ^{+0.10} _{-0.10}	0.79 ^{+0.41} _{-0.34}	>107	0.88	0.2	0.66	0.15	315 / 304	0
741*	1.91 ^{+0.21} _{-0.21}	1.11 ^{+0.97} _{-0.69}	>58	0.46	0.31	0.29	0.19	143 / 123	0
750	1.93 ^{+0.05} _{-0.05}	0.67 ^{+0.17} _{-0.16}	258 ⁺¹⁰⁷⁸ ₋₁₂₀	0.94	0.05	0.55	0.03	753 / 768	1
753	1.77 ^{+0.07} _{-0.07}	0.52 ^{+0.23} _{-0.21}	107 ⁺¹²³ ₋₃₉	1.85	0.57	1.11	0.34	510 / 539	1
754	1.96 ^{+0.05} _{-0.13}	1.18 ^{+0.67} _{-0.51}	>118	0.53	0.16	0.4	0.12	189 / 211	0
774	1.57 ^{+0.09} _{-0.09}	0.46 ^{+0.37} _{-0.26}	96 ⁺¹⁵² ₋₃₈	0.81	0.16	0.67	0.13	320 / 353	1
794	1.77 ^{+0.21} _{-0.21}	1.29 ^{+0.94} _{-0.69}	53 ⁺¹¹⁸ ₋₂₄	0.37	3.51	0.21	2.03	152 / 164	1
795	1.69 ^{+0.09} _{-0.09}	0.92 ^{+0.37} _{-0.33}	93 ⁺¹¹⁹ ₋₃₆	1.1	0.06	0.83	0.05	402 / 387	1
810	2.04 ^{+0.10} _{-0.11}	1.22 ^{+0.45} _{-0.48}	>171	0.56	0.54	0.36	0.35	238 / 252	0
815	1.91 ^{+0.12} _{-0.15}	0.62 ^{+0.61} _{-0.45}	>86	0.33	0.05	0.2	0.03	192 / 177	0
833*	1.79 ^{+0.27} _{-0.29}	0.89 ^{+1.04} _{-0.78}	>28	0.22	0.05	0.13	0.03	96 / 109	0
888	2.01 ^{+0.17} _{-0.20}	0.61 ^{+0.96} _{-0.44}	>60	0.23	0.38	0.13	0.22	94 / 110	0
905	1.90 ^{+0.09} _{-0.09}	0.87 ^{+0.36} _{-0.31}	>120	1.16	0.37	0.82	0.26	454 / 408	0
907	1.57 ^{+0.17} _{-0.09}	<0.54	>44	0.28	2.62	0.24	2.21	158 / 158	0
924	1.79 ^{+0.38} _{-0.12}	<1.21	>12	0.09	0.07	0.04	0.03	45 / 52	0
925	2.08 ^{+0.20} _{-0.24}	0.91 ^{+1.25} _{-0.77}	>47	0.28	0.27	0.15	0.14	86 / 94	0
948	1.75 ^{+0.07} _{-0.07}	0.68 ^{+0.24} _{-0.22}	66 ⁺³⁶ ₋₁₈	2.44	0.73	1.37	0.41	560 / 553	1
967	1.83 ^{+0.09} _{-0.09}	0.28 ^{+0.27} _{-0.23}	114 ⁺¹⁵⁹ ₋₄₄	1.61	44.73	0.76	22.07	418 / 460	1
984	1.65 ^{+0.03} _{-0.03}	0.18 ^{+0.08} _{-0.07}	96 ⁺²⁴ ₋₁₆	3.34	2.66	2.05	1.63	1151 / 1116	1
994	1.66 ^{+0.03} _{-0.03}	0.22 ^{+0.09} _{-0.08}	94 ⁺²⁵ ₋₁₆	4.39	3.26	2.81	2.1	1071 / 1031	1
1013	1.45 ^{+0.11} _{-0.11}	0.63 ^{+0.34} _{-0.29}	43 ⁺²⁰ ₋₁₁	0.82	1.39	0.64	1.12	304 / 310	1
1021	1.74 ^{+0.15} _{-0.15}	1.05 ^{+0.59} _{-0.48}	54 ⁺⁷⁶ ₋₂₂	0.53	0.09	0.32	0.06	220 / 202	1
1032	1.86 ^{+0.03} _{-0.03}	0.56 ^{+0.10} _{-0.09}	201 ⁺¹¹⁰ ₋₅₄	2.65	0.79	1.65	0.49	1173 / 1104	1
1041	1.84 ^{+0.11} _{-0.11}	0.81 ^{+0.38} _{-0.32}	68 ⁺⁶⁰ ₋₂₃	2.17	0.04	0.75	0.02	838 / 779	1
1042	2.19 ^{+0.04} _{-0.04}	0.91 ^{+0.17} _{-0.16}	70 ⁺²² ₋₁₄	2.17	0.04	0.75	0.02	838 / 779	1
1043	1.80 ^{+0.11} _{-0.11}	0.63 ^{+0.39} _{-0.34}	92 ⁺²⁴⁴ ₋₄₁	0.9	0.34	0.52	0.19	290 / 305	1
1046	1.72 ^{+0.02} _{-0.02}	0.56 ^{+0.06} _{-0.06}	99 ⁺¹⁵ ₋₁₁	3.78	0.02	2.53	0.02	1522 / 1475	1
1082	1.63 ^{+0.10} _{-0.06}	<0.28	91 ⁺⁴⁸ ₋₄₀	0.96	8.05	0.51	4.23	284 / 297	1
1084*	1.54 ^{+0.21} _{-0.23}	0.36 ^{+0.67} _{-0.34}	>36	0.35	0.18	0.28	0.15	99 / 98	0
1088	1.75 ^{+0.03} _{-0.03}	0.52 ^{+0.09} _{-0.08}	86 ⁺¹⁵ ₋₁₁	2.96	8.06	1.82	5.05	1115 / 1126	1
1090	1.71 ^{+0.01} _{-0.01}	0.38 ^{+0.04} _{-0.04}	75 ⁺⁷ ₋₆	4.74	1.29	2.98	0.82	1746 / 1591	1
1106	1.82 ^{+0.11} _{-0.11}	0.63 ^{+0.38} _{-0.33}	89 ⁺¹⁹⁹ ₋₃₈	1.05	0.64	0.57	0.35	313 / 326	1
1111	1.81 ^{+0.03} _{-0.03}	0.74 ^{+0.10} _{-0.09}	72 ⁺¹¹ ₋₉	3.16	0.15	1.93	0.09	1015 / 1075	1
1117	1.67 ^{+0.11} _{-0.11}	0.61 ^{+0.36} _{-0.31}	55 ⁺⁵⁰ ₋₁₉	1.03	0.15	0.63	0.09	305 / 289	1
1125	1.89 ^{+0.22} _{-0.24}	0.72 ^{+1.12} _{-0.54}	>40	0.24	3.05	0.15	1.89	107 / 108	0
1162	1.58 ^{+0.14} _{-0.14}	0.47 ^{+0.44} _{-0.36}	72 ⁺¹⁸⁶ ₋₃₃	0.44	0.06	0.34	0.05	191 / 187	1
1172	1.62 ^{+0.04} _{-0.03}	<0.09	77 ⁺¹⁹ ₋₁₄	5.95	5.83	3.38	3.33	831 / 856	1
1182	1.92 ^{+0.05} _{-0.05}	0.67 ^{+0.19} _{-0.18}	>244	2.98	0.18	1.97	0.12	686 / 688	0

Table 2. continued.

BAT obsID	Γ^a	R^a	$E_c^b(\text{keV})$	$F_{2-10 \text{ keV}}^a$	$L_{2-10 \text{ keV}}^b$	$F_{20-40 \text{ keV}}^a$	$L_{20-40 \text{ keV}}^b$	χ^2/dof	error id ^(e)
1381	1.84 ^{+0.22} _{-0.22}	0.89 ^{+0.95} _{-0.71}	56 ⁺²⁶¹ ₋₂₇	0.42	12.6	0.19	6.6	163 / 148	1
1471*	1.72 ^{+0.13} _{-0.13}	0.88 ^{+0.54} _{-0.44}	>81	0.43	0.11	0.36	0.09	197 / 223	0
1503*	1.63 ^{+0.16} _{-0.16}	0.65 ^{+0.38} _{-0.47}	>56	0.36	0.15	0.3	0.13	147 / 161	0
1536	1.47 ^{+0.12} _{-0.12}	0.61 ^{+0.40} _{-0.33}	60 ⁺⁴⁹ ₋₂₀	0.63	2.42	0.53	2.07	265 / 280	1
1581	1.73 ^{+0.23} _{-0.23}	0.66 ^{+0.96} _{-0.46}	>40	0.32	5.95	0.23	4.18	105 / 110	0

^a Un-absorbed flux in units of $\text{erg cm}^{-2} \text{s}^{-1}$

^b Un-absorbed luminosity in units of erg s^{-1}

^c Identifier for the high energy cut-off confidence interval estimation. A value of 0 denotes lower limit measurement, a value of 1 corresponds to a securely inferred value